Design of a Square Rotor Driven Pneumatic Stepper Actuator for MR-guided Therapy

Haipeng Liang[1], Wanli Zuo[2], Zion Tsz Ho Tse[1]
1. School of Engineering and Materials Science, Queen Mary University of London, London, E1 4NS
2. School of Mechanical Engineering and Mechanics, Ningbo University, 818 Fenghua Road, Ningbo, Zhejiang 315211, China

Abstract - Magnetic resonance imaging (MRI) has been widely used in the diagnostics and treatment of soft tissues due to its ability to acquire high-resolution images with outstanding contrast. Therefore, magnetic resonance (MR)-guided therapy and its supporting equipment, including MR-conditional sensors and actuators, have been developed rapidly. In this study, a non-magnetic pneumatic stepper motor was developed. The working principle was analyzed, and the theoretical static output torque was expressed mathematically. The driven part of the proposed design is a polygon rotor derived from the Wankel Engine. Besides, the outline of the inner wall of the housing was investigated. Experiments were conducted with the motor functioning at different speeds under different air pressures, by controlling the air in each chamber sequentially, the rotor can rotate continuously in dual directions with a torque of up to 38 mN·m and a maximum speed of 400 rpm. The MR test showed that no image artifact was found.

***Keywords* — Image-guided therapy, Magnetic resonance imaging (MRI), Pneumatic stepper motor.**

I. Introduction

With the magnetic field, MRI can image the nucleus in hydrogen since hydrogen has a high gyromagnetic ratio that produces a strong signal. Because soft tissues contain hydrogen-rich water and fat, MRI is capable of mapping the locations of soft tissues [1]. Compared with other imaging modalities, MRI can provide a higher tissue resolution and clearer images [2]. Unlike X-ray, computerized tomography (CT), ionizing radiation is not needed for its working [3], saving both patients and radiological staff from potential damage. As a result, MRI has been widely used in MR-guided treatments for cardiac electrophysiology (EP) therapy [4], [5], breast biopsy [6], and prostate interventions [7], [8]. Thus, interventional MRI has become an advanced technique for radiologists to guide medical instruments to diseased organs for diagnosis and treatment, which normally require the use of image-guided devices.

However, as MR generates a strong magnetic field, using ferromagnetic materials in and around the scanners can pose a risk to the device. Plus, the magnetic flux produced by paramagnetic materials placed inside the scanner can distort the magnetic field, lowering the image quality. For these reasons, medical devices that work under MRI must be MR-safe or MR-conditional [9], meaning that their design must be non-magnetic with minimal conductive components if any. As a result, motors driven by electromagnetic forces are not allowed to be used.

Various kinds of MR-conditional actuators have been developed, including piezoelectric [10, 11], hydraulic [12], and pneumatic actuators [13-15]. Although there is no magnetic material in a piezoelectric actuator, the electric current generated can emit electromagnetic interferences (EMI), which can significantly reduce the signal-to-noise ratio (SNR) [16], thereby deteriorating the image quality. Thus, radiofrequency (RF) shielding is needed in an MRI environment which would complicate the system. The work of hydraulic motors does not generate EMI, but the liquid leakage is unacceptable in clinical environments.

Unlike piezoelectric actuators, pneumatic actuators do not emit EMI during operation, so produce little SNR reduction under the MRI environment [17]. Additionally, Compressed air is available in MR rooms, and there is no risk of air leakage in the clinical environment [18]. Hence, pneumatic actuators have become an excellent choice for robots working under MRI.

For pneumatic motors driven by continuous airflow, control strategies for robotic systems are required for precise position and speed control [19-21]. Plus, components like sensors, encoders, and optical connectors are required for a closed control loop. All of these complicate the connection of the manipulator to the controller. In contrast, stepper motors can be controlled step by step using air sequences without incorporating any position feedback, thus significantly reducing the possibility of image deterioration.

Some stepper motors use cylinders to transfer the linear motion of pistons into linear or rotatory output [22], [23]. Secoli *et al*. designed a pneumatic stepper motor that is driven by three cylinders, in which trapezoidal thread was used to achieve linear movement [23]. But the configuration of three cylinders and lengthy thread make its volumetric dimension too large (250 mm × 250 mm × 50 mm), limiting its applications where a compact size is required. Although it can achieve an output torque of 400 N·mm at a relatively low speed of 10.8 rpm, the complex design complicates its fabrication and assembly. Another option is to use teeth as the driving parts which can produce great output power. The stepper motors designed by Groenhuis *et al*. can generate great output force and torque (330 N and 3700 mN·m) [24], which are the greatest among the presented designs. Sajima *et al*. designed an actuator through controlling the engagement of multiple face gears [15]. It has a high resolution of 4.29° and can generate a decent torque of 150 mN·m under 0.6 MPa, reducing the need for a

gearbox for high-resolution applications, but its maximum speed of around 48 rpm is low for many robots. All the listed designs are assembled with many components, therefore, it is desired to have a motor that uses fewer parts. This work introduces a motor with fewer fabricated components, making it one of the simplest designs. Besides, the use of seals can increase its output torque to 38 mN·m, and the use of a gearbox can increase its torque to fit most applications. Liang *et al.* recently proposed a cycloidal motor that has a simple design in which a maximum speed of 2000 rpm was achieved [25], which is the maximum among the listed designs. But it can generate a maximum output torque of 11 mN·m due to the air leakage. As a result, sealing the gaps between the moving parts is critical to enlarge the torque. However, different edges on the outer ring of the rotor are constantly in contact with the inner wall of the housing, making it difficult to seal the whole surface. In comparison, this motor has only four edges in contact with the inner wall of the housing, so it is much easier to seal the gaps. Furthermore, unlike the lens-shaped rotor, fabrication and accuracy control are much simpler with a square-shaped rotor. Last, a way to reduce the step size is proposed by attaching the output on the rotor, to obtain a higher resolution and better output performance.

According to the reported cycloidal motor, a type of pneumatic stepper motor is proposed, in which a ring gear rotates around a spur gear. A quadrangle rotor with four lateral edges is created, and the edges of the rotor can be sealed easily. As a result, the output torque is much larger than the cycloidal motor with a similar size. The contributions of this work are as follows: 1) simple mechanism structure with only four fabricated parts, low fabrication cost, and ease to assemble, 2) compact size of 64 mm × 70 mm × 22 mm, ease to get fitted with various robots, and 3) maximum output speed of 400 rpm, suitable for most applications in surgical robots. All the components used are non-metallic and non-conductive, making the motor MR-safe. The working principle and kinematics model are discussed, and the experiment shows that the output torque can reach 38 mN·m with a resolution of 120°.

II. Methods and Materials

Fig. 1 depicts the design of the pneumatic stepper motor, the number of moving parts is reduced to two (the rotor and shaft). The materials used are non-magnetic to meet the requirements of MR safety. To provide a clear view of the movement inside, the cover is made of transparent polymethyl methacrylate (PMMA) using laser cutting, which has a high resolution and a good surface finish. The three other fabricated parts are made of resin using 3D printing (Formlabs 3+), which has good precision and air tightness. All the standard bearings are made of polyamide and glass. Fig. 1a shows the photo of the motor, and Fig. 1b depicts a section view, showing that the stepper motor is composed of only seven parts, including three bearings.

The inner side of the housing is separated into three chambers by the rotor placed inside, and the volume of each chamber changes along with the rotation of the rotor. Three air holes are located at the same surface considering the ease of hose arrangement, and the channel routes are shown in Fig. 1c. Two airflow channels go around the housing wall to let the three inlets locate with a circumference difference of 120º (in red lines), then the compressed air is distributed into different chambers. Considering the long hoses (over 1 m), the influence of the hose length difference (5 cm) between different airflow channels is relatively low and can be neglected.

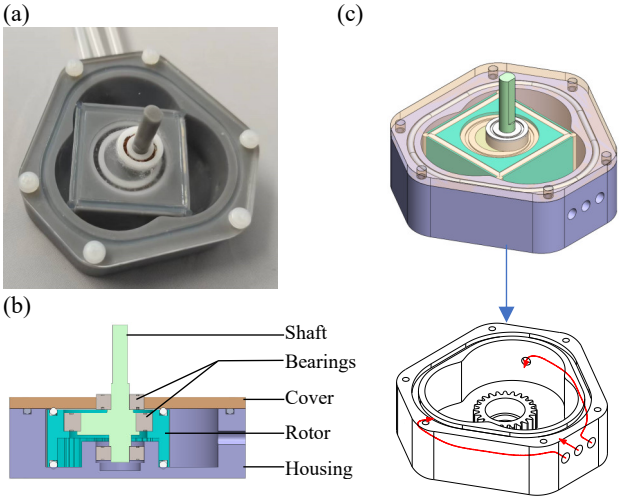

Fig. 1. (a) Photo of the stepper motor. (b) Section view of the motor. (c) 3D view of the motor and the airflow channels inside the housing.

The compressed air in the chambers drives the rotor to work, there are some gaps between the rotor and cover, rotor and housing. Therefore, it is important to minimize the gaps in the chambers to generate the full output force. Silicone strips were applied to the edges of the rotor, to create the closed chambers, and silicone oil was used to reduce the friction. Three 3/2-way pneumatic valves (Hoerbiger PS13950-636A) were applied to control the flow of compressed air in and out of three chambers.

A. Working Principle

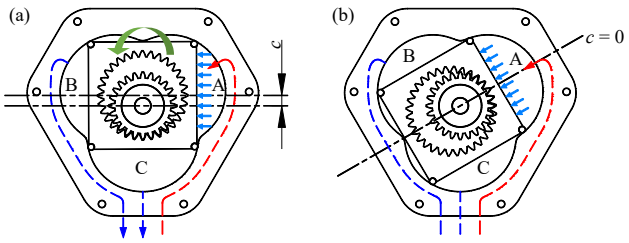

Fig. 2. (a) Start position of one step. (b) End position.

Fig. 2 shows the operation of compressed air in one chamber with the rotation of the rotor. The housing is separated into three chambers, Chamber A, B, and C. The rotor is in the shape of a quadrangle, and its rotation is guided by a pair of gears. The inner gear is mounted on the housing, and the ring gear on the rotor is engaged with and rotates around the inner gear. At the start position of one step (in Fig. 2a), the compressed air (shown as the red line) enters Chamber A and creates a force to drive the rotor to move. The blue dashed lines show the air exhaust from the other two channels, and the blue arrows

represent the force generated by the air applying to the rotor. As the rotor center is eccentric to the output shaft center at the start position, the air creates a torque to drive the rotor to rotate, and the moment arm at this point is denoted as c. Along with the rotation of the rotor, the moment arm and the torque decrease until the rotor stops at this position where the moment arm reaches zero (in Fig. 2b), at which time the volume of Chamber A reaches its maximum. The shaft generates a reverse torque in whichever direction it is moving towards, allowing the rotor to hold this position. Once this step is completed, the inlet of Chamber A becomes an outlet, allowing the air to exhaust in the next step. In this position, the adjacent surface of the rotor is just at the start position of Chamber B, where the moment arm is the greatest for the next step. Then, air entering Chamber B can drive the rotor to move to the next phase. Similarly, in the next phase of motion, the air in Chamber C drives the rotor to rotate by another 30°. In summary, air fills in and exhausts from three chambers in turn to generate the continuous rotation of the rotor and shaft.

The air pressure difference between the two adjacent chambers drives the quadrangle rotor to move toward the lower pressure side. Then, the rotation of the rotor can generate an output torque on the shaft. It is the eccentric shaft and planetary gear system that constrain the rotation of the quadrangle, instead of the inner wall of the housing. Therefore, the pressure between the housing wall and the rotor edges can be controlled by adjusting the compression ratio of the seals, reducing the abrasions between them.

Fig. 3 shows the status of compressed air in three chambers during a 12-step movement at a speed of 1 step/s, in which one chamber is activated at any given time and the rotation direction is controlled by adjusting the air sequence in different chambers.

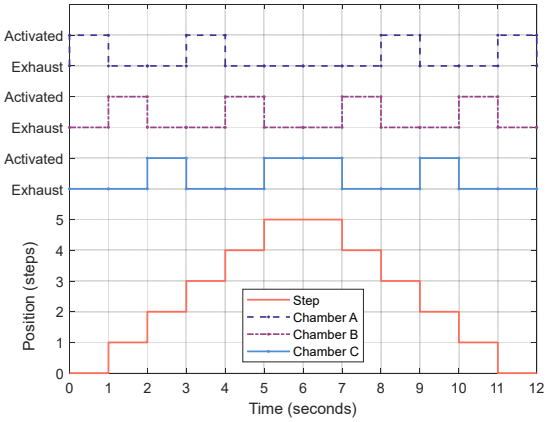

Fig. 3. Pneumatic actuation of three chambers during a 12-step movement.

Fig. 4 depicts the outline drawing of the rotor and inner wall of the housing, in which R is the radius from the rotor center to the outline of the housing, c is the eccentricity between the rotor center and output center, α is the rotation angle of the shaft, and h is the thickness of the rotor. All the parameters of the presented motor and their values are shown in Table 1.

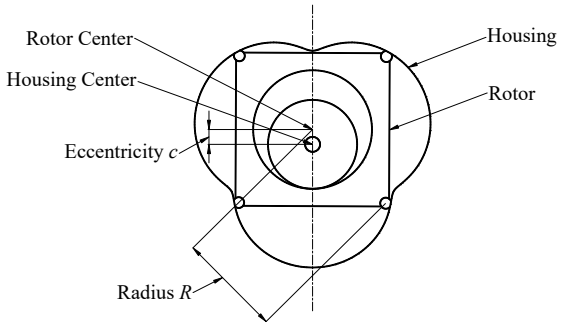

Fig. 4. Parameters in the motor.

Table 1. Descriptions of parameters

Parameter	Description	Value
W	Width	64 mm
H	Height	22 mm
i	Transmission ratio	1:4
c	Eccentricity	3.2 mm
R	Radius of the rotor	22.4 mm
h	Height of the rotor	16 mm
Z_K	Number of teeth of the ring gear	32
Z_I	Number of teeth of the inner gear	24
m	Modulus of the gear	0.8
α	Rotation angle of the shaft	-
n_H	Rotation speed of the inner gear	-
n_K	Rotation speed of the ring gear	-

B. Theoretical Calculations

In this design, the rotor fixed with the ring gear K rolls around the inner gear I on the housing, which is a planetary system. As the inner gear is fixed, the transmission ratio of the ring gear and carrier can be expressed as:

$$i = \frac{n_K}{n_H} = \frac{Z_K - Z_I}{Z_K} \quad (1)$$

where n_H and n_K denote the rotation speed of the carrier and ring gear, respectively, and Z_K and Z_I are the teeth numbers of the ring gear and inner gear. When

$$Z_K = 32, \text{ and } Z_I = 24,$$

the transmission ratio $i = \frac{n_K}{n_H} = \frac{1}{4}$, meaning that one cycle rotation of the ring gear results in four cycles of carrier rotation. Hence, the rotor rotates around the shaft at a speed of ω with an eccentricity of c, and it is also spinning around itself at a speed of $1/4 \cdot \omega$. As the rotation speed of the output shaft is four times that of the rotor, the rotation angle of the rotor is $1/4 \cdot \alpha$. In each 360° cycle, the rotor rotates by 90°, indicating that there are another three points on this outline with a circumference degree difference of 90°. Thus, the rotor has a quadrangle shape.

C. Theoretic & Realistic Profile

While the motor is running, the rotor is moving inside the chamber created by the housing and the cover. Due to the fabrication error and component deformation, there are some gaps between the moving parts, which in turn leads to air leakage. This air leakage can decrease the force applied and then reduce the output power. To obtain closed chambers, such gaps need to be well sealed. In this design, silicone strip seals with a diameter of 2 mm are mounted on the grooves of the top

and bottom faces of the rotor to seal both gaps (top and bottom seals in Fig. 5). Besides, to minimize the air leakage between different chambers, the lateral edges of the rotor are fabricated in the shape of round grooves to allow the silicone strips to be attached. Then, four lateral seals are placed at the four lateral edges.

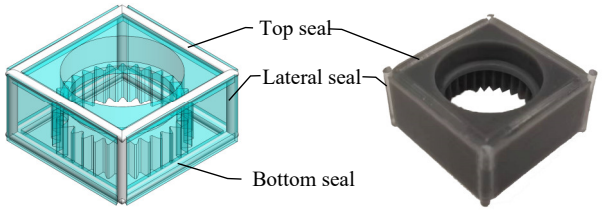

(a) (b)

Fig. 5. (a) Computer-aided design of the seals attached to the rotor. (b) Photo of the rotor with the silicone seals.

The centers of the lateral seals are at the four lateral edges, and the theoretic profile is the trajectory of the center point of the seal. Because of the four lateral seals, the realistic profile of the housing is offset by the theoretical profile. This offset equals the difference between the silicone seal radius and the seal compression amount.

In this study, a compression ratio of 15% is applied to the lateral seals. The realistic profile is the curve in contact with the seals as shown in Fig. 6a, in which o_3 is the seal center, o_2 is the rotor center, and P is the tangent point of the two pitch circles of the gear set. The angle between Po_3 and o_2o_3 is described as a swinging angle Φ.

The triangle showing the relationship between the swinging angle and other parameters is shown in Fig. 6b. Assuming the shaft rotates by α, then point o_3 on the rotor spins by $\frac{1}{4}\alpha$ around the rotor center. As a result, $\angle Po_2o_3$ is calculated as $(\pi - \frac{3}{4}\alpha)$. According to the law of cosines, in $\triangle Po_2o_3$ it can be expressed as:

$$\begin{cases} (4c)^2 = R^2 + f^2 - 2Rf \cdot \cos\Phi \\ f^2 = (4c)^2 + R^2 + 2 \times 4Rc \cdot \cos\frac{3}{4}\alpha \end{cases} \quad (2)$$

where f is the length of Po_3

According to the law of sines, it can be expressed as:

$$\frac{4c}{\sin\Phi} = \frac{f}{\sin\frac{3}{4}\alpha} \quad (3)$$

Based on Eqs. (2) - (3), the swinging angle Φ can be calculated as:

$$\begin{cases} \cos\Phi = \dfrac{R + 4c \cdot \cos\frac{3}{4}\alpha}{\sqrt{R^2 + 16c^2 + 8Rc \cdot \cos\frac{3}{4}\alpha}} \\ \sin\Phi = \dfrac{4c \cdot \sin\frac{3}{4}\alpha}{\sqrt{R^2 + 16c^2 + 8Rc \cdot \cos\frac{3}{4}\alpha}} \end{cases} \quad (4)$$

Assuming the diameter of the seal is a, because of the seal compression ratio of 15%, the circle with the center on the theoretical profile and edge on the realistic profile has a diameter of $\frac{17}{20}a$. Then, the realistic profile is expressed as:

$$\begin{cases} x = c \cdot \cos\alpha + R \cdot \cos\frac{1}{4}\alpha + \frac{17}{20}a \cdot \cos(\frac{\alpha}{4} + \Phi) \\ y = c \cdot \sin\alpha + R \cdot \sin\frac{1}{4}\alpha + \frac{17}{20}a \cdot \sin(\frac{\alpha}{4} + \Phi) \end{cases} \quad (5)$$

According to Eqs. (4) - (5), the realistic profile of the housing is calculated as:

$$\begin{cases} x = c \cdot \cos\alpha + R \cdot \cos\frac{1}{4}\alpha + \frac{17}{20}a \cdot \dfrac{R \cdot \cos\frac{\alpha}{4} + 4c \cdot \cos\alpha}{\sqrt{R^2 + 16c^2 + 8Rc \cdot \cos\frac{3}{4}\alpha}} \\ y = c \cdot \sin\alpha + R \cdot \sin\frac{1}{4}\alpha + \frac{17}{20}a \cdot \dfrac{R \cdot \sin\frac{\alpha}{4} + 4c \cdot \sin\alpha}{\sqrt{R^2 + 16c^2 + 8Rc \cdot \sin\frac{3}{4}\alpha}} \end{cases} \quad (6)$$

(a)

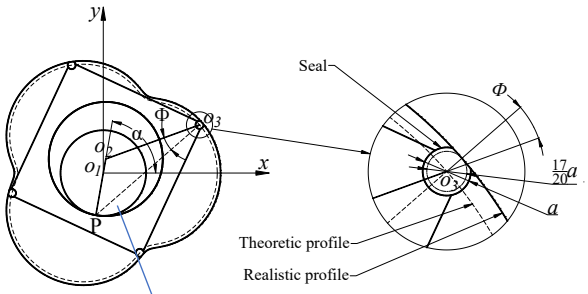

(b)

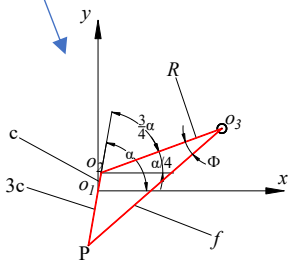

Fig. 6. (a) Schematic showing the contact status of the seal with the housing. (b) The triangle showing the swinging angle.

The purpose of developing theoretical models is to calculate the realistic profile considering the size of seals and their compression ratio, which is critical for model design and fabrication. In the following section, the theoretical output performance is calculated according to the airflow, friction, external load, and other factors that would affect the output performance. This mathematical model is used to analyze how different parameters affect the motor's performance.

D. Centripetal Acceleration Analysis

The sealing performance of the lateral seals is related to the force of the seals applied to the inner wall of the housing. This force is not only affected by the compression force of the seals but also the centrifugal force generated by the rotation of the rotor, which is related to the accelerated velocity. In Fig. 7, point A is the center of the rotor, and B is the cusp of the rotor. The centripetal acceleration of cusp B is a combination of the acceleration of A and the acceleration of B relative to A:

$$a_B = a_A + a_{BA}^t + a_{BA}^n \quad (7)$$

where

a_{B}, a_{A} – centripetal acceleration of points B and A,
$a_{\mathrm{BA}}^{\mathrm{t}}$ – tangential acceleration of point B relative to A, and
$a_{\mathrm{BA}}^{\mathrm{n}}$ – normal acceleration of point B relative to A.

Then, the maximum and minimum values of a_{B} happen when A, B, and center point *o* are in the same line, where the distances between B and *o* are the maximum and minimum. As the spinning speed of the rotor is one-fourth that of the rotation speed of the shaft, the maximum and minimum values of the acceleration of point B can be expressed as:

$$\begin{cases} a_{\mathrm{Bmax}} = \dfrac{\omega^2 R}{16} + \omega^2 c = \dfrac{\omega^2 c}{16}(K+16) \\ a_{\mathrm{Bmin}} = \dfrac{\omega^2 R}{16} - \omega^2 c = \dfrac{\omega^2 c}{16}(K-16) \end{cases} \tag{8}$$

where
a_{Bmax}, a_{Bmin} – the maximum and minimum values of the acceleration of point B,
ω – rotation speed of the shaft, and
K – the ratio of rotor radius R and eccentricity c.

Because $K = R/c = 7 < 16$, the minimum value of the accelerated velocity is negative, leading to a centrifugal force that takes the seals away from the inner wall of the housing which would reduce the sealing performance at these points. Therefore, the minimum compression force of the seals should be larger than this centrifugal force. Technically, the seal compression force is constant. Because of the variation of the centrifugal force, the abrasions on the inner wall of the housing also vary at different points. The centrifugal force arrives at the maximum at the trough points (red points in Fig. 7), then the abrasions of the housing inner wall at these points reach the greatest. Similarly, due to the negative centrifugal force at the crest points (blue points), the abrasions at these points are the weakest.

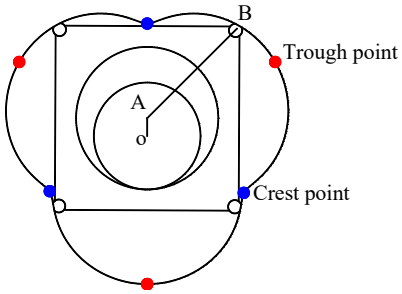

Fig. 7. Positions of the trough points and crest points.

E. Dynamic Model

The air mass flow shows the air consumption of the motor under different conditions. The air mass flow rate of the actuated and exhaust chambers $\dot{m}_{\mathrm{in}}$, $\dot{m}_{\mathrm{ex}}$ can be presented as [26], [27]:

$$\begin{cases} \dot{m}_{\mathrm{in}} = C_d C_o A_o f(p_r) \\ f(p_r) = \dfrac{P_s}{\sqrt{T_s}} \begin{cases} 1 & \dfrac{P_{\mathrm{atm}}}{P_s} < p_r < C_r \\ C_k\left[p_r^{2/k} - p_r^{(k+1)/k}\right]^{1/2} & C_r < p_r < 1 \end{cases} \\ C_k = \left[\dfrac{2}{k-1}\left(\dfrac{k+1}{2}\right)^{\frac{k+1}{k-1}}\right]^{\frac{1}{2}} = 3.864 \\ C_r = \left(\dfrac{2}{k+1}\right)^{\frac{k}{k-1}} = 0.528 \\ p_r = P_{\mathrm{in}}/P_s \end{cases} \tag{9}$$

where
$C_d = 0.8$ – discharge coefficient,
$C_o = 0.04$ – flow constant coefficient,
A_o – area of the orifice,
p_r – the ratio of chamber air pressure and inlet air pressure,
P_s – inlet air pressure,
$T_s = 293$ K – inlet air temperature,
$k = 1.4$ – specific heat constant,
P_{atm} – atmosphere air pressure, and
P_{in} – air pressure of the actuated chamber.

and

$$\begin{cases} \dot{m}_{\mathrm{ex}} = C_d C_o (-A_o) f(p_r) \\ f(p_r) = \dfrac{P_{\mathrm{ex}}}{\sqrt{T_o}} \begin{cases} 1 & \dfrac{P_{\mathrm{atm}}}{P_{\mathrm{ex}}} < p_r < C_r \\ C_k\left[p_r^{2/k} - p_r^{(k+1)/k}\right]^{\frac{1}{2}} & C_r < p_r < 1 \end{cases} \\ p_r = P_{\mathrm{e}}/P_{\mathrm{ex}} \end{cases} \tag{10}$$

where
P_{e} – exhaust air pressure,
P_{ex} – air pressure of the exhaust chamber, and
T_o – outlet air temperature.

When neglecting the air leakage, the mass flow rates in the compressible system are described as:

$$\begin{cases} \dot{m}_{\mathrm{in}} = \dfrac{P_{\mathrm{in}}}{R_g T_s}\dot{V}_{\mathrm{in}} + \dfrac{V_{\mathrm{in}}}{k R_g T_s}\dot{P}_{\mathrm{in}} \\ \dot{m}_{\mathrm{ex}} = -\dfrac{P_{\mathrm{ex}}}{R_g T_s}\dot{V}_{\mathrm{ex}} + \dfrac{V_{\mathrm{ex}}}{k R_g T_s}\dot{P}_{\mathrm{ex}} \end{cases} \tag{11}$$

where
R_g – gas constant,
T_s – supply temperature,
V_{in} – the volume of the chamber when the air flows in, and
V_{ex} – the volume of the exhaust chamber.

With Eqs. (7) – (9), the pressure changing rates are expressed as:

$$\begin{cases} \dot{P}_{\mathrm{in}} = \dfrac{k R_{\mathrm{g}} T_{\mathrm{s}}}{V_{\mathrm{in}}} C_{\mathrm{d}} C_{\mathrm{o}} A_{\mathrm{o}} f\left(\dfrac{P_{\mathrm{in}}}{P_{\mathrm{s}}}\right) - \dfrac{k P_{\mathrm{in}} \dot{V}_{\mathrm{in}}}{V_{in}} \\ \dot{P}_{\mathrm{ex}} = \dfrac{k R_{\mathrm{g}} T_{\mathrm{s}}}{V_{\mathrm{ex}}} C_{\mathrm{d}} C_o (-A_{\mathrm{o}}) f\left(\dfrac{P_{\mathrm{e}}}{P_{\mathrm{ex}}}\right) + \dfrac{k P_{\mathrm{ex}} \dot{V}_{\mathrm{ex}}}{V_{\mathrm{ex}}} \end{cases} \tag{12}$$

Considering the volume of one chamber, it can be filled in within a short time. Hence, the pressure deviation can be considered as 0, and the air pressures are expressed as:

$$\begin{cases} P_{\text{in}} = \dfrac{R_g T_s}{\dot{V}_{\text{in}}} C_d C_o A_o f\left(\dfrac{P_{\text{in}}}{P_s}\right) \\ P_{\text{ex}} = -\dfrac{R_g T_s}{\dot{V}_{\text{ex}}} C_d C_o A_o f\left(\dfrac{P_e}{P_{\text{ex}}}\right) \end{cases} \tag{13}$$

The generated torque τ is provided by the difference of compressed air in the intake and exhaust ports, and it can be calculated as:

$$\begin{aligned} \tau &= P_{\text{in}} \cdot V_{\text{in}} - P_{\text{ex}} \cdot V_{\text{ex}} \\ &= J \cdot \ddot{\alpha} + b_f \dot{\alpha} + M_f(\dot{\alpha}) + \tau_{\text{ld}} \end{aligned} \tag{14}$$

where
J – inertia of the motor,
b_f – damping coefficient,
$M_f(\dot{\alpha})$ – friction torque, and
τ_{ld} – external load.

Then, the dynamic model can be expressed as:

$$\ddot{\alpha} = J^{-1}\left[\frac{R_g T_s}{\dot{V}_{\text{in}}} C_d C_o A_o f\left(\frac{P_{\text{in}}}{P_s}\right) \cdot V_{\text{in}} + \frac{R_g T_s}{\dot{V}_{\text{ex}}} C_d C_o A_o f\left(\frac{P_e}{P_{\text{ex}}}\right) \cdot V_{\text{ex}} - b_f \dot{\alpha} - M_f(\dot{\alpha}) - \tau_{\text{ld}}\right] \tag{15}$$

Next, it can be simplified as:

$$\ddot{\alpha}(t) = \mathrm{A}(\dot{\alpha}) + \mathrm{B}(\alpha) + \mathrm{C} \tag{16}$$

where
$\mathrm{A}(\dot{\alpha}) = [-b_f \dot{\alpha} - M_f(\dot{\alpha})]/J$,
$\mathrm{B}(\alpha) = \left[\frac{R_g T_s}{\dot{V}_{\text{in}}} C_d C_o A_o f\left(\frac{P_{\text{in}}}{P_s}\right) \cdot V_{\text{in}} + \frac{R_g T_s}{\dot{V}_{\text{ex}}} C_d C_o A_o f\left(\frac{P_e}{P_{\text{ex}}}\right) \cdot V_{\text{ex}}\right]/J$,
$\mathrm{C} = -\tau_{\text{ld}}/J$.

Friction in the motor is regarded as LuGre model [28], which is the combining effect of static and dynamic friction forces. Due to the fabrication and assembly issue, the friction force at different positions varies. Besides, it is changing along with the sliding velocity of two contacted surfaces. Thus, the friction force is with respect to the rotation angle and speed. The friction torque $M_f(\dot{\alpha})$ in Eq. (14) is described as:

$$\begin{cases} M_f(\dot{\alpha}) = \sigma_0 z + \sigma_1 \dot{z} + \sigma_2 \dot{\alpha} \\ \dot{z} = [1 - \sigma_0 \cdot z \cdot g(\dot{\alpha}) \cdot \mathrm{sgn}(\dot{\alpha})]\dot{\alpha} \\ g(\dot{\alpha}) = [F_d + (F_s - F_d)e^{-[|\dot{\alpha}|/v_s]^2}]^{-1} \end{cases} \tag{17}$$

where
σ_0, σ_1, σ_2 – stiffness, micro damping, and viscous damping,
z – friction dynamic state,
v_s – velocity of the Stribeck friction,
F_d – Coulomb friction, and
F_s – static friction.

The volumes of chambers can be expressed as:

$$\begin{cases} V_{\text{in}} = V_{\text{in,init}} + \int \dot{V}_{\text{in}}\, dt \\ V_{\text{ex}} = V_{\text{ex,init}} + \int \dot{V}_{\text{ex}}\, dt \end{cases} \tag{18}$$

where $V_{\text{in,init}}$, $V_{\text{ex,init}}$ are the initial volumes of the chambers.

In Eq. (16), the volume of each chamber with respect to the rotating angle α can be obtained from the 3D model. Fig. 8 shows the volume change of three chambers in a one-step movement when compressed air fills in Chamber A. Due to the action of compressed air, the volume of Chamber A increases and that of Chamber C decreases until Chamber A arrives at its maximum, with an air expansion ratio of 5.328 / 3.072 = 1.73. When arriving at 60º, Chamber B reaches its minimum, and the volumes of Chamber A and C equal. At the same time, one lateral edge of the rotor is just at port B, separating it into two chambers. Chamber B is generated with one edge of the rotor and the outline of the housing, after passing 60º, the chamber connected to port B changes to the one generated by the adjacent edge of the rotor and the inner wall of the housing, and its volume starts increasing until the end of this step.

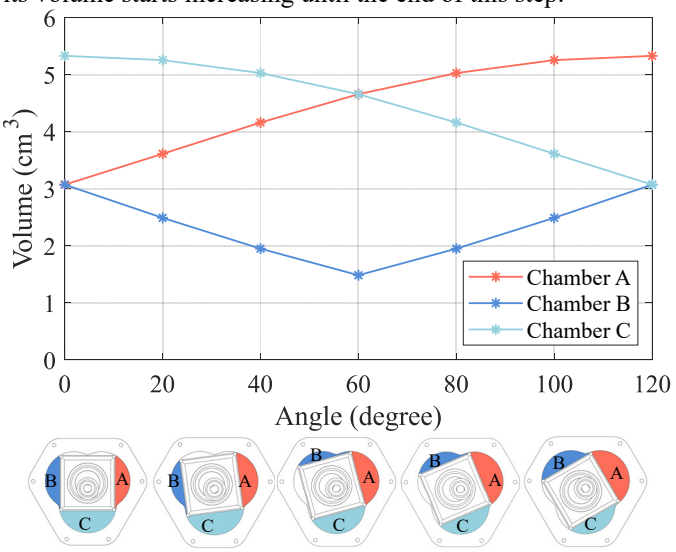

Fig. 8. Volume change in different chambers during one-step movement.

F. *Flange Output*

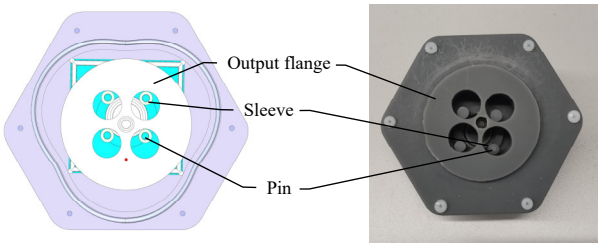

(a) (b)

Fig. 9. Motor with output flange attached to the rotor.

As the rotation step size of the rotor is 30º, the output can be attached to the rotor directly for a higher resolution. As shown in Fig. 9, four pins on the rotor are fitted with four sleeves which are tangent with the four holes on the output flange, then the flange can rotate along with the rotor at a speed that equals the spining speed of the rotor, and the spinning speeds of the pins relative to the small holes on the flange equal the rotating speed of the center shaft. Therefore, the output flange has a resolution of 30º rather than 120º of the center shaft. The sleeves are employed to decrease the friction between the pins and the flange; theoretically, using bearings can have this friction reduced even more, but would enlarge the overall size. The output torque of the flange is larger than the center shaft due to its higher resolution and lower speed. In order to have the closed chambers and keep space for the four pins and their

rotation, the rotor has a large size with a radius of 34 mm, resulting in an overall size of 94 mm × 103 mm × 33 mm. A prototype was fabricated using 3D printing (in Fig. 9b), showing that this flange has a higher resolution rotation.

III. Results

A. Experiment Setup

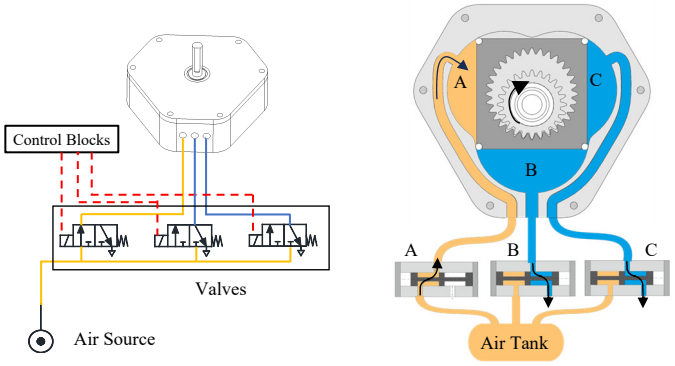

(a) (b)

Fig. 10. Diagram of the pneumatic system.

Fig. 10a shows the pneumatic valves connected to the motor, in which the motor is powered by the compressed air sequence. Three valves can generate three air sequences, which can get in and out of the relevant chambers in turn to drive the motor to rotate. Fig. 10b indicates the air flowing in and out of the motor from three valves, where valve A is activated (in amber shading) through which the compressed air goes into Chamber A and air in the other two chambers escapes from valves B and C (in blue shading). These valves do not generate any magnetic field and can be placed inside the MRI room.

In the current design, the flanged motor has a higher resolution, but the extra components bring added friction, lowering its output performance, so in this experiment, the motor was tested without the flange.

B. Torque Performance

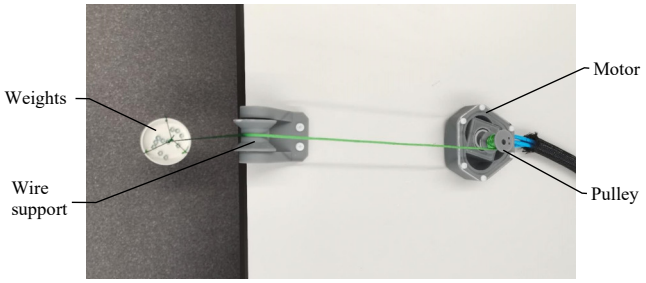

Fig. 11. Experimental set up for torque measurement.

The output torque was tested at different speeds under four different pressures. As shown in Fig. 11, a pulley system coupled with a shaft capable of lifting the container was used to measure the torque. The output torque can be obtained by varying the number of weights in the lifting container.

In the experiment, due to the friction resistance caused by the silicone seals, the minimum pressure to set the motor in motion was 0.28 MPa. Therefore, the output torque was measured at air pressures of over 0.35 MPa. Fig. 12 shows the output torque with respect to speed and air pressure. The maximum torque it can achieve is 38 mN·m at a speed of 50 rpm and a pressure of 0.55 MPa. In this study, because the parts are 3D printed and the seals are manually attached to the rotor, although the chambers are sealed, there are still some air leakages around the rotor in different chambers, which lowers its output. Additionally, the friction caused by the seals and air exhaustion also reduces its output torque.

It can be observed that when the speed increases, the torque drops rapidly. This is because the air driven into the chambers and hoses does not fill the whole chamber quickly enough to generate full pressure before the next air sequence applied to the rotor arrives. The compressed air in the long air hoses causes a low-pass filter effect to dampen the pressure waves [13], leading to the reduction of the output.

In this study, silicone is compressed at a rate of 15%, the experiment shows that lowering the compression ratio can reduce the friction of the rotor and increase its maximum working speed. However, the low compression ratio lowers the sealing performance, thus reducing the output torque. The optimization of the compression ratio is a balance between the output torque and the maximum speed. Also, seals made of materials with lower hardness and lower friction coefficients are worth trying. Various MR-safe materials can be considered, such as graphite, polytetrafluoroethylene (PTFE), silicone, nitrile rubber, etc. Graphite would generate small particles that can go into the valve, which is prohibited in the clinical environment. Nitrile rubber, which has a higher hardness, is typically used for high-pressure sealing and could generate a greater abrasion force with the inner wall of the housing, so it is unsuitable for this air-driving motor. PTFE could be considered with a high-accuracy fabrication process. Currently, considering the air pressure, ease of assembly, and fabrication process, silicone seals with a shore hardness of 50A are applied.

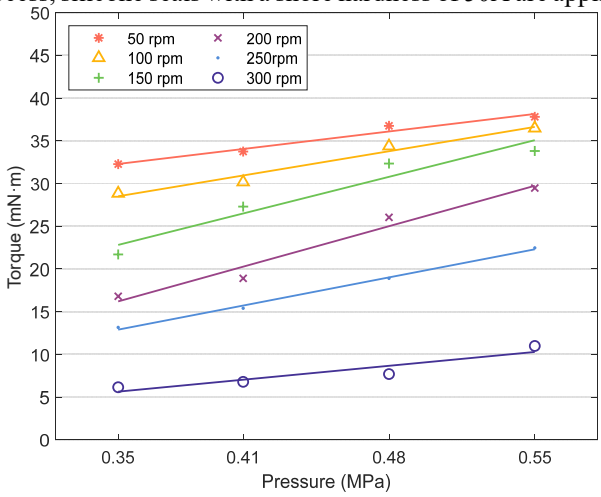

Fig. 12. Output torque with respect to rotation speed and air pressure.

C. Step Response

Step response shows the response time of the motor when compressed air is applied to the chamber and generates a force on the rotor, and it reveals the activation speed. In this experiment, a commercial encoder (LPD3806-600BM-G5-24C, Wisamic) coupled with the output shaft was used to measure

the rotation angle. The rotating speed was controlled by regulating the air sequence applied to different chambers. The rotation angle of the output shaft corresponding to time was acquired at three different speeds under two air pressures of 0.28 MPa and 0.55 MPa.

Fig. 13 shows the step response at three speeds (60 rpm, 100 rpm, and 200 rpm). Several observations have been found. First, the motor has a slower response when running under a lower pressure. This is because higher-pressure air fills in the chambers more quickly and generates a greater force on the rotor, driving it to rotate faster. Second, when compared to running at a faster speed (200 rpm), a steady state is found at the end of each step. This is due to the compressed air from the following chamber coming to activate the rotor before the current step is completed when operating at higher speeds, resulting in the absence of steady states. In Fig. 13a, the mean settling time is measured as 71.6 ms under 0.28 MPa and 47.3 ms under 0.55 MPa, with calculated bandwidths of 14 Hz and 21 Hz, respectively, indicating that the maximum speeds the motor can achieve under these two pressures are 14 steps/s and 21 steps/s when neglecting the friction change caused by the increased speed. Furthermore, all the step movements are shown as an overdamped system, overshoot does not occur because the large friction damps its movement. This friction force also limits the maximum speed. Finally, positioning errors are observed in the steady states, and this will be further analyzed in the following section.

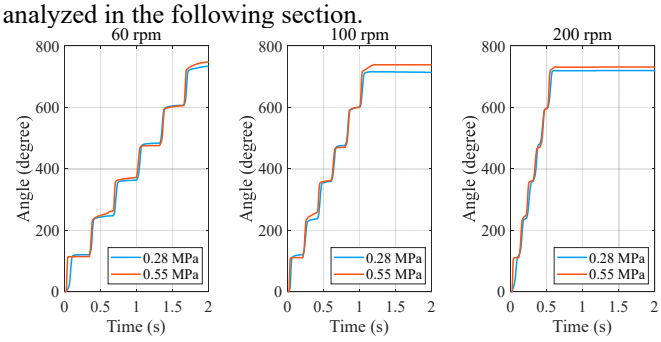

Fig. 13. Step response of the motor working under two air pressures at different speeds: (a) 60 rpm, (b) 100 rpm, (c) 200 rpm.

D. Error Analysis

Each step movement can drive the rotor to rotate by 30º, so twelve targeted positions were selected to calculate the positioning error with the rotor rotating for one full cycle. The error at each point was obtained from the mean value of three samples to minimize the influence of manual measurement.

Fig. 14 shows the errors of twelve target points under two air pressures at a speed of 60 rpm, at which the steady positions can be obtained at the end of each step. It is observed that the motor has a smaller error when working under a higher air pressure. This is because the higher-pressure air drives the rotor to overcome the friction force more easily and arrive at a more precise position. The torque decreases along with the increase of rotation angle until it is lower than the friction force, and the lower pressure reduces this torque. A maximum error of -22.6° was observed at the sixth step under the pressure of 0.35 MPa. This is most likely caused by the fabrication and assembly issue, leading to the unexpected friction change at this point. Because of the friction force, the rotor stops before reaching the target position at low speeds, thus the majority of errors are distributed negatively. Moreover, some peak points are found in this error pattern, which are significantly greater than the average value, indicating that the motor has a greater friction force at these points. The maximum error is about 18.8% of one step size (120°) and is acceptable for its use in robots. Plus, the use of a gearbox can have this error reduced. Another way to reduce the error is to use a fabrication method with higher accuracy to have the gears engaged better. Furthermore, the gaps in the bearings can also affect the trajectories of the rotor lateral edges and result in an extra force on the seal. Therefore, preloading the bearings helps to improve positioning accuracy.

Currently, this error pattern is for low speeds only. When running at high speeds, the rotor can pass the inlet port of the following step more easily to let the compressed air activate the rotor due to the inertia of the rotor and load.

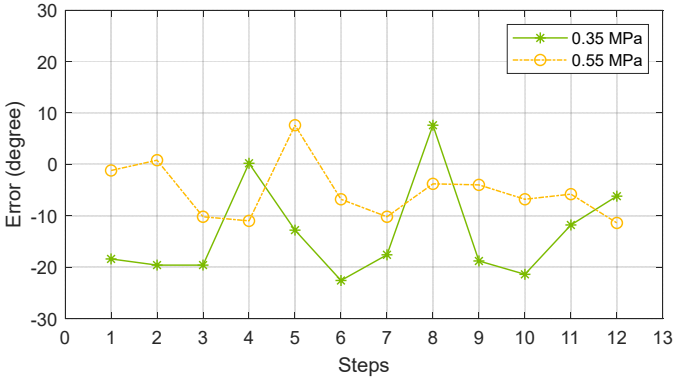

Fig. 14. Error distribution of three targets with respect to different air pressures.

E. MR Evaluation

The materials used in this motor are PMMA and grey resin, both are non-magnetic and non-conductive, meaning that this motor is intrinsically MR-safe. An MR test was conducted under a 3T MR scanner, in which the motor was immersed in a water bath. According to ASTM F2119 [29], an image artifact is defined with a pixel density variation exceeding 30% when the device is placed inside the MR scanner. Fig. 15 shows the MR images of the motor at different scan heights, indicating that there is no obvious image artifact caused by the motor.

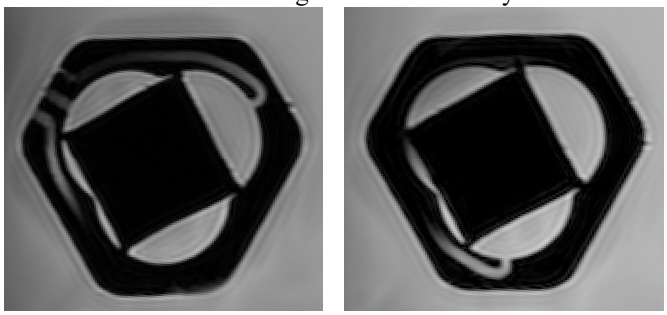

Fig. 15. Images of the motor inside the MR scanner.

IV. Discussion

Compared with the reported designs, the most significant benefit of the motor presented in this paper is its simple design, which has the fewest fabricated components of four among all the designs, significantly simplifying its assembly. Currently, it can achieve a decent torque of 38 mN·m which is relatively low, but this can be enlarged when coupling with a gearbox. Moreover, its maximum speed of 400 rpm is suitable for the majority of robot applications. Because of the use of seals, its maximum speed is lower than that of the cycloid motor by Liang *et al* [25], but its output torque is much greater, which broadens its applications.

The use of silicone seals can reduce the air leakages between different chambers which significantly increases the output torque. However, the seals also bring extra friction and lead to a significant energy loss although lubrication oil is applied. As the fabricated parts are made using 3D printing which has a relatively low accuracy, some seals may not be attached to the rotor properly, leading to some unexpected air leakages. Using components with higher accuracy can have its output improved. Another way to enhance the torque is to increase the thickness of the motor to enlarge the effective working area on the rotor while keeping the flange the same, allowing the flange of the gearbox to remain unchanged.

In the experiment, the air hoses have to be no more than 3 m to activate the motor due to the friction. Lowering the compression ratio of the seals allows for the use of longer air hoses, but the air leakages caused can decrease the torque as well. Apex seals and side seals with plastic bearings can be considered in the future for better sealing performance [30]. Finally, optical fibers can be fitted to obtain position feedback if a close-loop control is required, which can be used to track and compensate for the missing steps [31].

At present, the designs of the housing inner wall and rotor take into account the seals' airtightness, friction, and the highest operating speed. Future endeavors will center on refining the geometries, drawing from the friction model and centripetal acceleration, to minimise seal compression variability and realize the motor's peak performance. Additionally, while components produced via 3D printing offer limited precision, employing a more accurate fabrication technique, like CNC machining, could diminish the sealing discrepancies and enhance the motor's output efficacy.

V. Conclusion

This study presents a type of non-magnetic pneumatic motor used in an MR environment, and its output performance under different air pressures is analyzed. As the driving part is a rotor, its working requires few parts, making it easy to fabricate and assemble. The experiment shows that it has a maximum output torque of 38 mN·m and a maximum speed of 400 rpm, which shows the potential for its use in MR-safe robots. Future work will focus on optimizing the model and well-sealing the internal gaps to achieve higher torques and smoother rotations, and research on motors with more than three chambers would be worthwhile.

VI. Acknowledgments

This study was supported in part by the Academy of Medical Sciences Professorship, Royal Society Wolfson Fellowship, Cancer Research UK (EDDPMA-Nov21\100026), and the National Institutes of Health (NIH) Bench-to-Bedside Award. This study was also supported by the NIH Center for Interventional Oncology: Grant ZID# BC011242 & CL040015, the Intramural Research Program of the National Institutes of Health, and the China Scholarship Council (No. 20200830071).

The authors would like to thank Mr. Mike Angus for his assistance with the 3D printing and laser cutting parts.

References

[1] D. I. Hoult, and B. Bhakar, "NMR signal reception: Virtual photons and coherent spontaneous emission," *Concepts in Magnetic Resonance,* vol. 9, no. 5, pp. 277-297, 1997/01/01, 1997.

[2] S. W. Hetts, M. Saeed, A. J. Martin, L. Evans, A. F. Bernhardt, V. Malba, F. Settecase, L. Do, E. J. Yee, A. Losey, R. Sincic, P. Lillaney, S. Roy, R. L. Arenson, and M. W. Wilson, "Endovascular Catheter for Magnetic Navigation under MR Imaging Guidance: Evaluation of Safety In Vivo at 1.5T," *American Journal of Neuroradiology,* vol. 34, no. 11, pp. 2083, 2013.

[3] S. Stapf, "D. W. McRobbie, E. A. Moore, M. J. Graves and M. R. Prince. MRI—from picture to proton. Cambridge University Press, Cambridge, 2003, pp. 359 paperback. ISBN 0-521-52319-2," *Magnetic Resonance in Chemistry,* vol. 42, no. 10, pp. 905-905, 2004/10/01, 2004.

[4] K.-W. Kwok, Y. Chen, T. C. P. Chau, W. Luk, K. R. Nilsson, E. J. Schmidt, and Z. T. Tse, "MRI-based visual and haptic catheter feedback: simulating a novel system's contribution to efficient and safe MRI-guided cardiac electrophysiology procedures," *Journal of Cardiovascular Magnetic Resonance,* vol. 16, no. 1, pp. O50, 2014/01/16, 2014.

[5] P. Bhagirath, M. van der Graaf, R. Karim, K. Rhode, C. Piorkowski, R. Razavi, J. Schwitter, and M. Gotte, "Interventional Cardiac Magnetic Resonance Imaging in Electrophysiology Advances Toward Clinical Translation," *Circulation-Arrhythmia and Electrophysiology,* vol. 8, no. 1, pp. 203-211, Feb, 2015.

[6] L. Liberman, N. Bracero, E. Morris, C. Thornton, and D. D. Dershaw, "MRI-Guided 9-Gauge Vacuum-Assisted Breast Biopsy: Initial Clinical Experience," *American Journal of Roentgenology,* vol. 185, no. 1, pp. 183-193, 2005/07/01, 2005.

[7] G. S. Fischer, I. Iordachita, C. Csoma, J. Tokuda, S. P. DiMaio, C. M. Tempany, N. Hata, and G. Fichtinger, "MRI-Compatible Pneumatic Robot for Transperineal Prostate Needle Placement," *IEEE/ASME Transactions on Mechatronics,* vol. 13, no. 3, pp. 295-305, 2008.

[8] J. G. R. Bomers, J. P. M. Sedelaar, J. O. Barentsz, and J. J. Futterer, "MRI-Guided Interventions for the Treatment of Prostate Cancer," *American Journal of Roentgenology,* vol. 199, no. 4, pp. 714-720, Oct, 2012.

[9] A. Standard, "F2503. Standard practice for marking medical devices and other items for safety in the magnetic resonance environment," *ASTM International, West Conshohocken, PA*, 2013.

[10] Z. T. H. Tse, H. Elhawary, M. Rea, B. Davies, I. Young, and M. Lamperth, "Haptic Needle Unit for MR-Guided Biopsy and Its Control," *IEEE/ASME Transactions on Mechatronics,* vol. 17, no. 1, pp. 183-187, 2012.

[11] Y. X. Liu, W. S. Chen, P. L. Feng, and J. K. Liu, "A rotary piezoelectric motor using bending vibrators," *Sensors and Actuators a-Physical,* vol. 196, pp. 48-54, Jul 1, 2013.

[12] Z. Y. Guo, Z. Y. Dong, K. H. Lee, C. L. Cheung, H. C. Fu, J. D. L. Ho, H. K. He, W. S. Poon, D. T. M. Chan, and K. W. Kwok, "Compact Design of a Hydraulic Driving Robot for Intraoperative MRI-Guided Bilateral Stereotactic Neurosurgery," *Ieee Robotics and Automation Letters,* vol. 3, no. 3, pp. 2515-2522, Jul, 2018.

[13] D. Stoianovici, A. Patriciu, D. Petrisor, D. Mazilu, and L. Kavoussi, "A New Type of Motor: Pneumatic Step Motor," *IEEE/ASME Transactions on Mechatronics,* vol. 12, no. 1, pp. 98-106, 2007.

[14] K. Chinzei, R. Kikinis, and F. A. Jolesz, "MR Compatibility of Mechatronic Devices: Design Criteria." pp. 1020-1030.

[15] S. Hiroyuki, K. Hiroki, K. Kenta, D. Takeyoshi, and M. Ken, “MR-Safe Pneumatic Rotation Stepping Actuator,” *Journal of Robotics and Mechatronics,* vol. 24, no. 5, pp. 820-827, 2012.
[16] K. Masamune, E. Kobayashi, Y. Masutani, M. Suzuki, T. Dohi, H. Iseki, and K. Takakura, “Development of an MRI-Compatible Needle Insertion Manipulator for Stereotactic Neurosurgery,” *Journal of Image Guided Surgery,* vol. 1, no. 4, pp. 242-248, 1995/01/01, 1995.
[17] G. S. Fischer, A. Krieger, I. Iordachita, C. Csoma, L. L. Whitcomb, and G. Fichtinger, "MRI Compatibility of Robot Actuation Tech3niques – A Comparative Study." pp. 509-517.
[18] R. Gassert, A. Yamamoto, D. Chapuis, L. Dovat, H. Bleuler, and E. Burdet, “Actuation methods for applications in MR environments,” *Concepts in Magnetic Resonance Part B: Magnetic Resonance Engineering,* vol. 29B, no. 4, pp. 191-209, 2006/10/01, 2006.
[19] Y. Wang, H. Su, K. Harrington, and G. S. Fischer, “Sliding Mode Control of Piezoelectric Valve Regulated Pneumatic Actuator for MRI-Compatible Robotic Intervention,” 2010, pp. 23-28.
[20] C. Bergeles, P. Vartholomeos, L. Qin, and P. E. Dupont, "Closed-loop commutation control of an MRI-powered robot actuator." pp. 698-703.
[21] G. S. Fischer, “Enabling technologies for MRI guided interventional procedures,” Ph.D., The Johns Hopkins University, Ann Arbor, 2009.
[22] H. Liang, and Z. T. H. Tse, “An Opposed Piston Driving Pneumatic Stepper Motor for MR Intervention Robotics,” *IEEE/ASME Transactions on Mechatronics*, pp. 1-11, 2023.
[23] R. Secoli, M. Robinson, M. Brugnoli, and F. Rodriguez y Baena, “A low-cost, high-field-strength magnetic resonance imaging-compatible actuator,” *Proc Inst Mech Eng H,* vol. 229, no. 3, pp. 215-24, Mar, 2015.
[24] V. Groenhuis, and S. Stramigioli, “Rapid Prototyping High-Performance MR Safe Pneumatic Stepper Motors,” *IEEE/ASME Transactions on Mechatronics,* vol. 23, no. 4, pp. 1843-1853, 2018.
[25] H. P. Liang, and Z. T. H. Tse, “Cycloidal Stepper Motor: A Systematic Approach for Designing a Nonmagnetic Rotary Actuator,” *Ieee-Asme Transactions on Mechatronics,* vol. 28, no. 1, pp. 71-79, Feb, 2023.
[26] J. H. Wang, J. S. Pu, and P. Moore, “A practical control strategy for servo-pneumatic actuator systems,” *Control Engineering Practice,* vol. 7, no. 12, pp. 1483-1488, Dec, 1999.
[27] S. Y. Chen, and S. S. Gong, “Speed tracking control of pneumatic motor servo systems using observation-based adaptive dynamic sliding-mode control,” *Mechanical Systems and Signal Processing,* vol. 94, pp. 111-128, Sep 15, 2017.
[28] D. R. Lin, X. Y. Wang, G. L. Yang, S. Yuan, and Q. Q. Sun, “Adaptive robust control for fully electric pitch system of tank with dynamic friction compensation,” *Journal of Mechanical Science and Technology,* vol. 36, no. 10, pp. 4967-4978, Oct, 2022.
[29] F. ASTM, "2119–01. Standard Test Method for Evaluation of MR Image Artifacts from Passive Implants," 2014.
[30] S. Zhang, J. X. Liu, Z. X. Zuo, and Y. Zhang, “An analytical investigation of oil film thickness for the apex seal in a small Wankel rotary engine,” *Tribology International,* vol. 116, pp. 383-393, Dec, 2017.
[31] Z. T. H. Tse, H. Elhawary, A. Zivanovic, M. Rea, M. Paley, G. Bydder, B. L. Davies, I. Young, and M. U. LampÉrth, “A 3-DOF MR-Compatible Device for Magic Angle Related In Vivo Experiments,” *IEEE/ASME Transactions on Mechatronics,* vol. 13, no. 3, pp. 316-324, 2008.

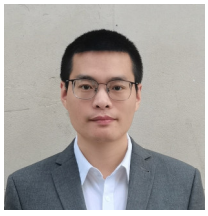

Haipeng Liang received his B.S. degree in mechanical engineering from Harbin Institute of Technology, Harbin, China. He is currently working toward the Ph.D. degree in medical engineering with the School of Engineering and Materials Science, Queen Mary University of London, UK.

His research interests include medical robotics, MR conditional actuators and sensors.

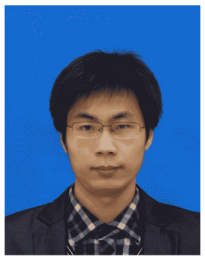

Wanli Zuo received his B.S. degree and M.S. degree in mechanical engineering and automation from Nanjing Tech University, Nanjing, China, and Ph.D. in vehicle engineering from Southeast University, Nanjing, China.

He is a Lecturer at Ningbo University, Ningbo, China. He was an academic visitor in Medical Robotics at the University of York, and an academic visitor in Digital Health & Robotics at Queen Mary University of London. His research interests include damping in resonators, medical robotics, and automotive electronics.

Zion Tsz Ho Tse is an Academy of Medical Sciences Professor in Digital Health & Robotics and the Director of the Centre for Bioengineering at Queen Mary University of London. Prior to that, he was a Chair Professor at the University of York, and an Associate Professor at the University of Georgia. Before that, he was a research fellow at Harvard University, Boston, Massachusetts. His PhD degree in Mechatronics in Medicine was received from Imperial College London in the UK. Most of his academic and professional experience has been in AI, Digital Health, Medical Robotics and Imaging. He has been developing and testing a broad range of medical technologies in his career, most of which have been applied in clinical patient trials. His research bridges Engineering and Medicine, connecting multidisciplinary teams of medical doctors, researchers and engineers.